ELSEVIER

Journal of Structural Geology 30 (2008) 177–193

JOURNAL OF STRUCTURAL GEOLOGY

www.elsevier.com/locate/jsg

The analogue shear zone: From rheology to associated geometry

Christoph E. Schrank*, David A. Boutelier, Alexander R. Cruden

Department of Geology, University of Toronto, 22 Russell Street, Toronto, ON, M5S 3B1 Canada

Received 6 April 2007; received in revised form 3 November 2007; accepted 8 November 2007
Available online 17 November 2007

Abstract

The geometry of ductile strain localization phenomena is related to the rheology of the deformed rocks. Both qualitative and quantitative rheological properties of natural rocks have been estimated from finite field structures such as folds and shear zones. We apply physical modelling to investigate the relationship between rheology and the temporal evolution of the width and transversal strain distribution in shear zones, both of which have been used previously as rheological proxies. Geologically relevant materials with well-characterized rheological properties (Newtonian, strain hardening, strain softening, Mohr–Coulomb) are deformed in a shear box and observed with Particle Imaging Velocimetry (PIV). It is shown that the width and strain distribution histories in model shear zones display characteristic finite responses related to material properties as predicted by previous studies. Application of the results to natural shear zones in the field is discussed. An investigation of the impact of 3D boundary conditions in the experiments demonstrates that quantitative methods for estimating rheology from finite natural structures must take these into account carefully.

Keywords: Physical modelling; Analogue modelling; Shear zones; Rheology; Strain distribution

1. Introduction

It is well known from field observations (e.g., Bayly, 1970; Lamouroux et al., 1994; Fusseis et al., 2006), experiments (Biot et al., 1961; Abbassi and Mancktelow, 1992; Treagus and Sokoutis, 1992; Hudleston and Lan, 1994; Kenis et al., 2004, 2005), and analytical theory (Biot, 1957, 1961; Ramberg, 1962; Schmid et al., 2004) that geometrical features of ductile strain localization phenomena (e.g., folds, shear zones, deformed clasts in conglomerates, mullions) are related to the rheological properties of the deformed rocks. Hence, both qualitative (Means, 1984, 1995; Hull, 1988; Lamouroux et al., 1994; Fusseis et al., 2006) and quantitative (Bayly, 1970; Talbot, 1999a,b; Treagus, 1999, and references therein; Treagus and Treagus, 2002; Kenis et al., 2005) attempts have been made to derive rheological information (power-law exponents, relative viscosities, and general material behaviour such as strain softening or hardening) from deformed natural rocks.

However, in nature observed finite structures, especially those that evolved to large length scales such as crustal shear zones, are likely the result of a complex deformation history. Clear overprinting relationships must be present to derive a well-constrained spatiotemporal history which is essential for the inference of mechanical information (e.g., Means, 1995). Another concern is the low-strain rate of viscoplastic geological processes. Ambient parameters influencing rheology such as temperature, pressure, fluid content and mineral composition will likely change over sufficiently long time scales (e.g., Means, 1995). The progressive acquisition of a new structure (e.g., fabric) produces new anisotropies in the deformed rock, probably leading to changes in mechanical properties and localization geometry (Cobbold et al., 1971; Cosgrove, 1989). Additional complexity arises due to the scale dependence of strain localization (Paterson, 2001; Schrank et al., in press) and its sensitivity to boundary and initial conditions (Garstecki et al., 2003).

In this paper we investigate whether meaningful qualitative rheological constraints can be deduced from geometrical features of shear zones that develop in a single, isochoric,

* Corresponding author. Tel.: +1 416 978 0833; fax: +1 416 978 3938.
E-mail address: schrank@geology.utoronto.ca (C.E. Schrank).

0191-8141/$ - see front matter © 2007 Elsevier Ltd. All rights reserved.
doi:10.1016/j.jsg.2007.11.002

isothermal, isochemical, continuous, deformational event without changes in deformation mechanism and bulk strain rate. We performed physical experiments in a shear box with a variety of isotropic materials (Newtonian, strain hardening/softening, Mohr–Coulomb) whose rheological properties have been determined independently with appropriate instruments (i.e., TA AR1000 controlled-stress rheometer and a modified Hubbert-type shear apparatus (Hubbert, 1951)). Our materials are regarded as isothermal analogues for simplified macroscopic rheological end members in nature. The experiments were observed with a Particle Image Velocimetry system (PIV) that allows the determination of displacement and strain fields at high spatiotemporal resolution. Incremental and cumulative (i.e., finite) deformation histories are compared.

Our investigation focuses on the temporal evolution of shear zone width and transversal strain distribution, both of which have been used previously as qualitative (e.g., Means, 1984, 1995; Hull, 1988; Jessell and Lister, 1991; Lamouroux et al., 1994; Fusseis et al., 2006) or quantitative (e.g., Talbot, 1999b; Treagus, 1999) rheological proxies. Means (1984, 1995) and Hull (1988) predicted that shear zones in strain-hardening materials should widen with time (Fig. 1A). On the other hand, the actively deforming part of shear zones in softening materials should narrow progressively (Fig. 1B). Consequently, the transversal strain distribution in hardening shear zones should become less heterogeneous (i.e., flat-topped), whereas softening shear zones should display more heterogeneous strain profiles over time (Means, 1995; Lamouroux et al., 1994). It is shown that qualitative predictions concerning (a) shear zone narrowing/widening as a function of material softening/hardening (Means, 1984, 1995; Hull, 1988) and (b) the evolution of transversal strain distribution quantified by the strain localization intensity parameter, I_{loc} (Schrank et al., in press), are confirmed by our experiments. I_{loc} is a simple measure of the heterogeneity of the shear strain distribution (Fig. 1C,D). However, an investigation of the impact of boundary conditions on strain distribution demonstrates that generic quantitative methods for determining rock rheology from finite structures are likely to fail if these boundary conditions are not carefully considered in the applied method (e.g., Sonder, 2001).

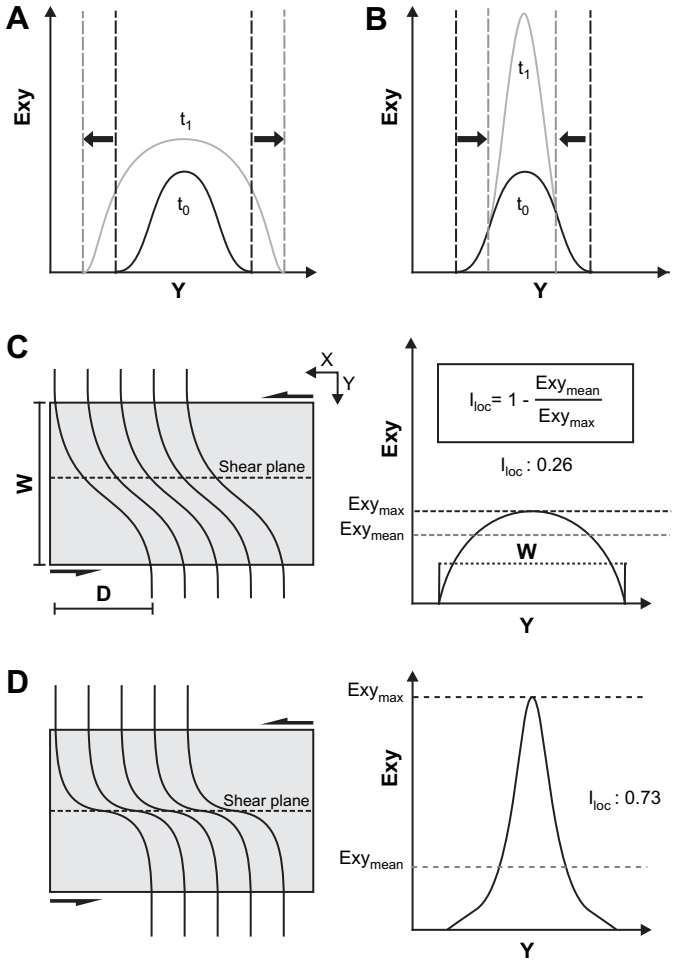

Fig. 1. [A] Conceptual sketch of the finite strain profile evolution of a shear zone in a strain-hardening material assuming constant bulk strain rate. A precursory shear zone at time t_0 (black line) reached a critical strain in its centre, after which strain hardening occurs. Hence, deformation in the next time increment (t_1, grey line) propagates outwards into the host rock. The shear zone widens and the strain distribution becomes less heterogeneous. [B] Sketch of the finite strain profile evolution of a shear zone in a strain-softening material assuming constant bulk strain rate. At time t_0, strain softening begins in the shear zone centre. As a result, the centre can accommodate more strain in the next time increment t_1. The zone of active deformation decreases, the shear zone narrows, and the finite strain distribution becomes more heterogeneous. [C] and [D] illustrate the strain localization intensity parameter, I_{loc} (after Schrank et al., in press). At the left, two shear zones, depicted by passive markers (solid black lines), have identical width W and finite displacement D but different strain distributions. The corresponding conceptual strain profiles are plotted on the right. The shear zone in [C] exhibits a less heterogeneous strain distribution. Hence I_{loc} is small due to a high ratio of Exy_{mean} to Exy_{max}. The shear zone in [D] displays a more heterogeneous strain distribution. I_{loc} is large due to a small ratio of Exy_{mean} to Exy_{max}.

2. Experimental setup

The experiments were conducted in a simple shear box (Fig. 2). Box dimensions are $30 \times 20 \times 4$ cm ($x \times y \times z$). A basal cut parallel to x in the box centre serves as a sharp velocity discontinuity. Hence, one half of the box is displaced horizontally by a piston with respect to the stationary second half. The piston is driven smoothly by a stepper motor at a rate of 1 cm/hour, which is a typical laboratory rate for scaled physical experiments using Silicon polymers such as PDMS (Polydimethylsiloxane, Weijermars, 1986). For convenience, the experiment with sand ran at a rate of 2 cm/hour because its Mohr–Coulomb rheology is time-independent. Total displacement is 5 cm for each experiment.

For each material, the experiment was repeated three times. Since the results were robust, we show only one experiment for each material. The experiments have been observed from above with a Particle Imaging Velocimetry (PIV) system (LaVision GmbH). PIV enables the derivation of displacement fields by cross-correlation of sequential images at high spatiotemporal resolution (see Adam et al., 2005, for a detailed description of the PIV technique). The displacement field is the basis for further strain calculations. We used a single monochrome CCD camera oriented normal to and about 1 m above the surface of the experiment. Images were recorded

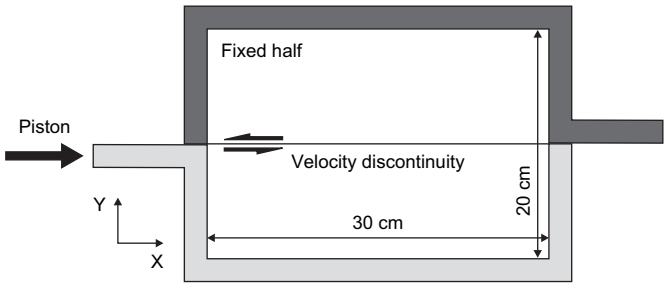

Fig. 2. Plan view sketch of the shear box. Box inner depth is 4 cm.

every 10 min (image recording frequency for Carbopol experiment was one image per 12 min and for sand one image per 6 min). The experiment surface is covered with marker particles to enhance the quality of correlation. The camera resolution is 1600 by 1200 pixels. The image resolution ranges between 50 and 60 pixels/cm with a typical calibration error of 0.4 pixels. Search window sizes of 64 square pixels with 50% overlap were chosen for the final step of the multipass correlation (using LaVision software DaVis 7). In other words, we derived about four displacement vectors per square centimetre (Fig. 3). See Table 1 for estimated errors in the PIV measurements and the Appendix for their derivation.

3. Boundary conditions

We employed ductile and granular materials in this study. The former adhere to the walls and the base of the shear box. Hence, no-slip boundary conditions hold for the box boundaries, whereas the surface is a free-slip boundary. In any standard experiment, the shear box is filled up to a height of 2 cm, which ensures that the width of the evolving shear zone is sufficiently small compared to the width of the shear box. To examine the impact of boundary conditions, we also varied the filling height, and ran experiments in which the material was decoupled from the box bottom by a 2 cm layer of low-viscosity corn syrup (see Section 7).

In our experiments, shear localization is forced and strongly influenced by the kinematic boundary conditions: namely, the linear velocity discontinuity at the bottom of the box, the no-slip conditions at the box surfaces, the box geometry, and the constant imposed displacement velocity. This is a drawback of the experimental method since these boundary conditions apply restrictions on how shear zones can evolve in the models. The velocity discontinuity defines the location of the shear zone while the box geometry and the no-slip conditions control maximum shear zone width as well as the longitudinal width distribution. The constant-velocity boundary conditions impose a limit on possible strain rates. Shear zones originating from material instabilities rather than kinematic boundary conditions exhibit a richer spectrum of geometries. Such natural geometries reflect the rheology of the underlying materials better and, in some ideal cases, might even provide reasonable quantitative rheological estimates.

In this paper we do not intend to derive a method to invert quantitative rheological data from natural shear zone geometries. However, our results have some implications for such inversion attempts which are discussed in Section 8. As mentioned above, we investigate whether qualitative predictions regarding the relation between material properties and shear zone width as well as the shape of the transversal shear strain distribution can be confirmed experimentally (e.g., Hull, 1988; Means, 1995). This requires that localization has already occurred and we do not attempt to model shear zone nucleation. The well-controlled boundary conditions of our experimental setup allow us to isolate the effect of material rheology on shear zone width and strain distribution. Constant-velocity boundary conditions are suitable for modelling of plate-driven shear zones and are common in geodynamic studies (Regenauer-Lieb and Yuen, 2003). We demonstrate and discuss the profound influence of the kinematic boundary conditions on strain distributions in Section 7.

Shear apparatus with basal velocity discontinuities have been used successfully to study shear deformation in analogue models for almost a century (e.g., Cloos, 1928; Riedel, 1929; Tchalenko, 1970; Naylor et al., 1986; Cobbold et al., 1991; McClay and Bonora, 2001). Alternative experimental setups are difficult to realize. Sufficient spontaneous localization due to material instabilities in isothermal Newtonian and power-law softening materials would have to be induced by prescribing weak mechanical heterogeneities that also would influence the localization pattern and would result in structures with more complex kinematics (e.g., Grujic and Mancktelow, 1998). Nevertheless, it is shown that our model shear zones exhibit a characteristic response with respect to the deformed material even though localization is strongly governed by boundary conditions.

4. Parameters

To better understand the relevance of finite field data, we investigate the incremental and cumulative geometrical evolution of our model shear zones. The parameters used here are (a) shear zone width, (b) maximum and mean shear strain, (c) displacement, and (d) strain localization intensity I_{loc}. The derivation of these parameters from our experiments is outlined below.

In the first step, the incremental displacement field is determined by cross-correlation of two sequential images for all images of a given experiment (Fig. 3A, see Adam et al., 2005, for a detailed explanation of the PIV technique). The cumulative displacement fields are obtained by summing the incremental data. Shear strain, Exy (Fig. 3B), is calculated from both incremental and cumulative displacement fields using:

$$\mathrm{Exy} = \frac{\mathrm{d}D_x}{\mathrm{d}y} \tag{1}$$

where D_x is displacement in x-direction. The transversal (i.e., y-direction) shear strain profile is then determined in the box centre for both incremental and cumulative Exy maps (Fig. 3B). This was done to minimize boundary effects due to the moving rear and front walls of the box such as corner

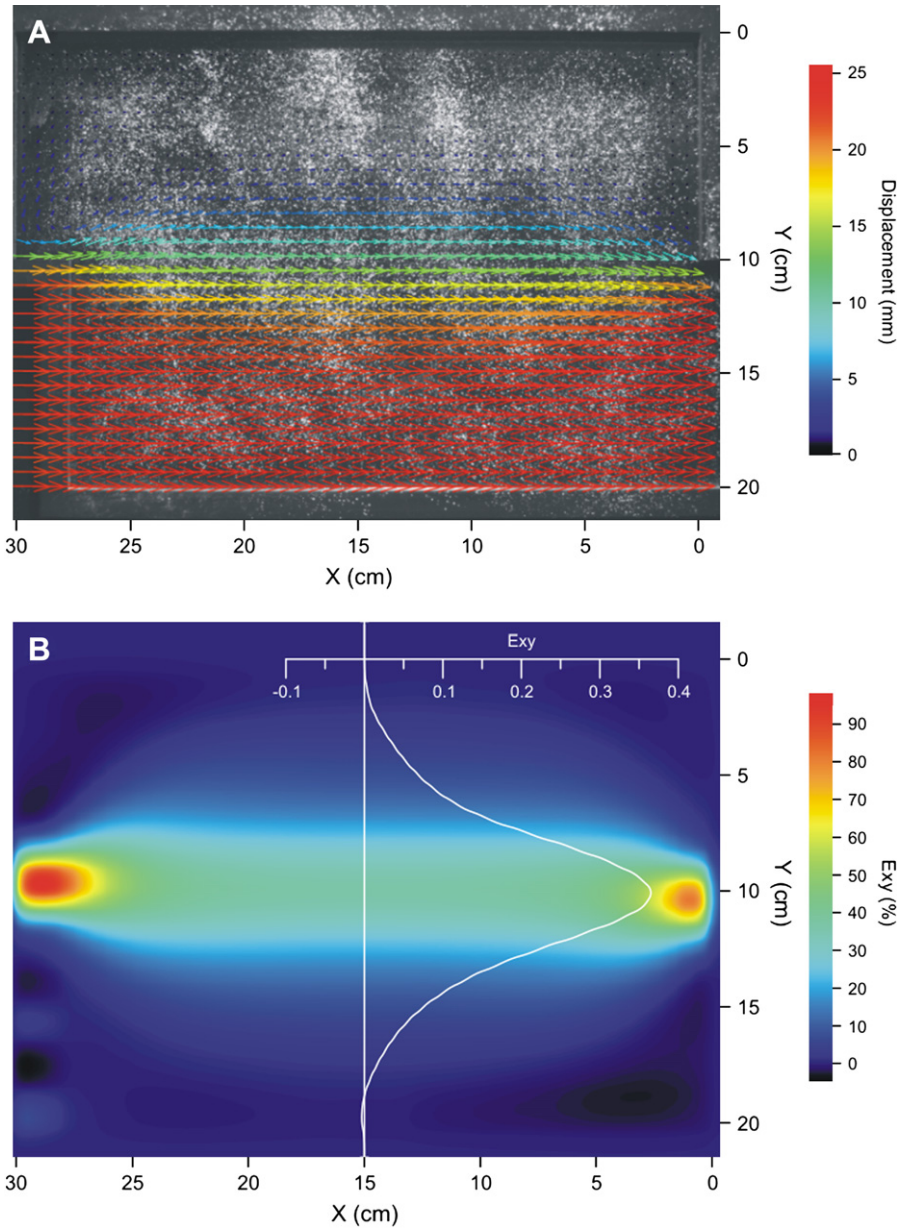

Fig. 3. Cumulative displacement field for PDMS experiment [A] and map of cumulative shear strain with transversal shear strain profile in box centre [B] calculated from displacement field in [A]. Note the corner flow and strain concentrations at the shear zone ends due to box boundaries. White marker particles (see [A]) were sifted over model surface to enable PIV correlation.

flow (Fig. 3). In order to obtain a continuous strain profile, the strain values are smoothly interpolated over the search windows. From the shear strain profiles the total shear zone width, W, is calculated as the distance bracketed by the shear zone boundaries. The latter are given by the condition (with respect to maximum Exy along that profile, i.e., the shear zone centre, Fig. 4):

$$\frac{\mathrm{dExy}}{\mathrm{d}y} = 0 \tag{2}$$

The bulk displacement, D, accommodated along the profile is easily obtained by integrating the shear strain profile in between the shear zone boundaries (Ramsay and Graham, 1970). The maximum shear strain, $\mathrm{Exy}_{\max}$, is the maximum of the corresponding profile (Fig. 4). The mean shear strain, $\mathrm{Exy}_{\mathrm{mean}}$, is calculated from (Ramsay and Graham, 1970):

$$\mathrm{Exy}_{\mathrm{mean}} = \frac{D}{W} \tag{3}$$

I_{loc} is defined as (Schrank et al., in press):

$$I_{\mathrm{loc}} = 1 - \frac{\mathrm{Exy}_{\mathrm{mean}}}{\mathrm{Exy}_{\max}} \tag{4}$$

I_{loc} is a measure of the heterogeneity of the strain distribution. It tends to zero for less localized strain profiles with a flat, broad top (Fig. 1C) and converges to unity for very localized profiles with a narrow peak over a broad base (Fig. 1D).

Table 1
Empirically determined displacement and strain measurement errors for cumulative (upper row) and incremental (lower rows) data

Material	Imposed displacement rate (cm/s)	Observed displacement rate (cm/s)	Absolute displacement error per time step (cm)	Absolute strain error
Cumulative data				
PDMS	2.727E−04	2.729E−04	1.13E−04	0.0003
P80PL20	2.873E−04	2.772E−04	6.08E−03	0.0200
Carbopol	2.711E−04	2.622E−04	6.39E−03	0.0136
Sand	5.252E−04	5.082E−04	6.12E−03	0.0187

Material	Imposed displacement rate (cm/s)	Observed mean displacement rate (cm/s)	Standard deviation for observed mean displacement rate	Deviation from imposed displacement rate (%)
Incremental data				
PDMS	2.727E−04	2.706E−04	1.129E−05	−0.77
P80PL20	2.873E−04	2.766E−04	1.025E−05	−3.74
Carbopol	2.711E−04	2.642E−04	9.840E−06	−2.57
Sand	5.252E−04	5.133E−04	3.029E−05	−2.27

Material	Imposed displacement per time step (cm)	Observed maximum displacement error per time step (cm)	Maximum deviation from imposed displacement (%)	Absolute strain error
PDMS	0.1636	0.0102	6.23	0.030
P80PL20	0.1724	0.0159	9.22	0.052
Carbopol	0.1952	0.0064	3.28	0.014
Sand	0.1891	0.0251	13.26	0.077

For explanation of parameters see Appendix.

Small-scale strain fluctuations may occur on the margins of the shear strain profiles (compare Fig. 11). This is due to a number of reasons. First, technical issues render displacement field determination more challenging close to the box boundaries. Corner flow in the viscous materials affects the outermost regions of the box leading to local strain reversals next to the walls. Finally, inherent experimental and correlation errors (see Appendix) also cause fluctuations. Consequently, additional minima and maxima can occur at the profile margins resulting in small-scale oscillations in the total width determination due to its dependence on the criterion given in Eq. (2). To avoid this noise, we additionally determined another shear zone width, W', bracketed by points y_1 and y_2 at which (Fig. 4):

$$\mathrm{Exy}(y_{1,2}) = \frac{1}{3}\mathrm{Exy}_{\max} \tag{5}$$

W' is less sensitive to the aforementioned bias and will be shown to comply with the evolution of W.

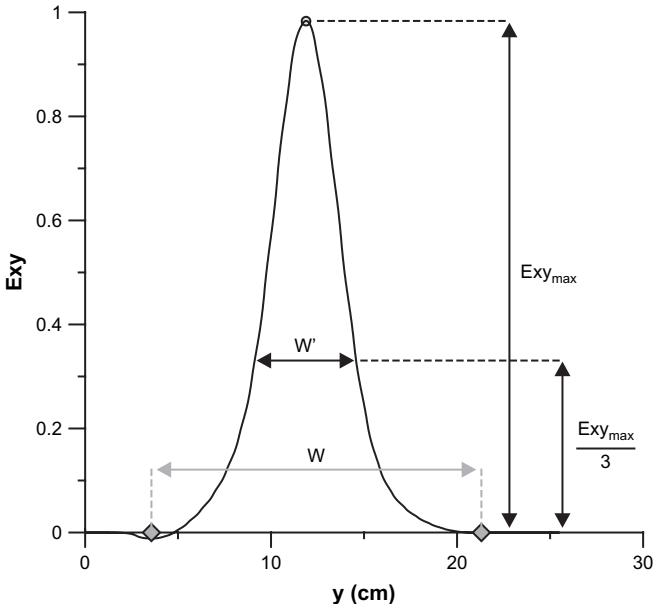

Fig. 4. Parameters used for shear zone characterization. Note local strain reversal at the left boundary (grey diamond) due to corner flow. For explanation see text.

5. Materials

We investigated four materials, which represent common end member materials employed in analogue and numerical modelling of rock deformation: (1) a Newtonian fluid (PDMS, Weijermars, 1986), (2) a viscoelastic strain hardening, strain-rate softening material (a mixture of 80 vol.% PDMS and 20 vol.% Plasticine, referred to as P80PL20), (3) a viscoelasto-plastic (pseudoplastic) strain-softening material (Carbopol, a polyacrylic acid polymer), and (4) a Mohr–Coulomb material (quartz sand). The rheology of the fluids and Carbopol has been measured with a controlled-stress rheometer (see Boutelier et al., in press). The properties of the sand have been determined with a modified Hubbert-type shear apparatus (Hubbert, 1951; Lohrmann et al., 2003). We measured six loads per test and repeated each measurement five times to reduce errors.

(1) Newtonian materials exhibit a linear relation between strain rate and stress and are generally used for modelling diffusion creep (e.g., Ranalli and Fischer, 1984; Poirier, 1985). PDMS has a constant viscosity of 2.5×10^4 Pa s in the range of typical experimental strain rates. A power-law regression confirms the linear relation between

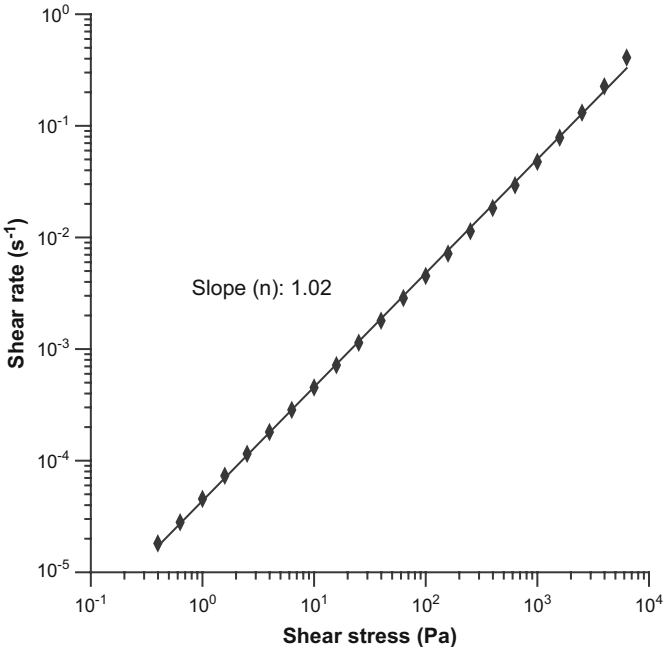

Fig. 5. Results of steady state flow test for PDMS. Note the linear relation between shear strain rate and stress with an exponent of approximately 1.

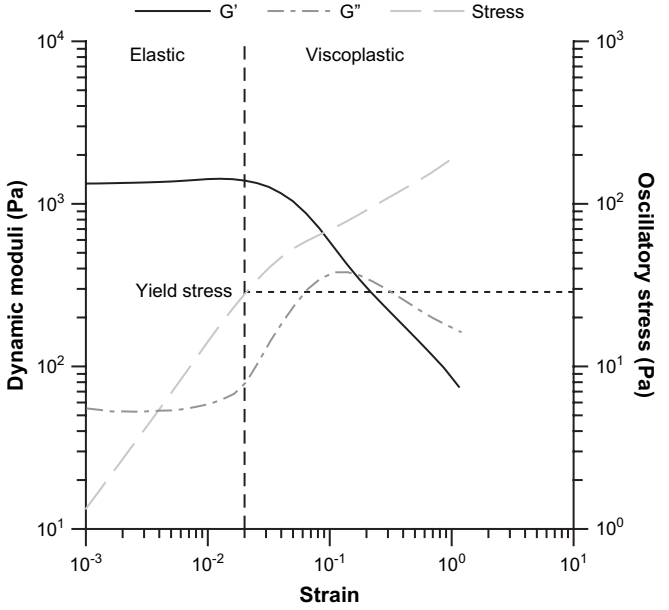

Fig. 6. Results of strain sweep test for Carbopol at 10^{-3} rad/s. Material behaviour changes drastically at 2% strain, after which the dynamic elastic storage modulus G' decreases whereas the dynamic (viscous) loss modulus G'' increases. The material is purely elastic before failure, becomes elastoplastic at failure, and elastoviscoplastic after about 20% strain. For a detailed explanation of the measurement procedure and the dynamic moduli see Boutelier et al. (in press).

stress and strain rate measurements yielding a best-fit stress exponent, n, of 1.02 (Fig. 5) for:

$$\sigma^n = \eta\dot{\varepsilon} \tag{6}$$

Stress is denoted by σ, $\dot{\varepsilon}$ is strain rate, and η is a viscosity constant.

(2) The strain-hardening material, P80PL20, is a mixture of PDMS and Harbutt's Plasticine (white). Its rheology is quite complex and explained in detail by Boutelier et al. (in press). For stresses $\leq$70 Pa, viscosity increases non-linearly with strain. Above this threshold stress, P80PL20 enters a quasi-linear domain approximately behaving as a power-law strain-rate softening fluid with a stress exponent of 2.8. However, our experiments remain in the non-linear, low-stress, strain-hardening domain due to the low bulk strain rate.

(3) Carbopol Ultrez 10 is a cross-linked polymer in powder form that, once hydrated, forms a 3D network of closely packed microgels with a pseudoplastic rheology (Noveon, 1995). We mixed 5% by weight with water without adding neutralizer (pH $\sim$ 3). The material behaves elastically until ca. 2% strain (Fig. 6). At this strain, pseudoplastic yielding occurs at a shear stress of about 30 Pa followed by rapid strain softening resulting in viscoplastic flow. Once damaged, Carbopol behaves like a power-law strain-rate softening fluid with a stress exponent of ca. 5. This behaviour is commonly used for modelling rocks deforming by dislocation creep (e.g., Evans and Kohlstedt, 1995).

(4) We used quartz sand (#505 Silica 50 M from Bell & McKenzie Ltd.) with an average grain size of 200 μm which is a common analogue (e.g., Schellart, 2000) for a Mohr–Coulomb material. The Mohr–Coulomb law is often employed to describe the behaviour of the upper crust (Byerlee, 1978). However, sand does not behave like an ideal cohesionless Coulomb material with constant frictional properties but exhibits transitional strain hardening followed by strain softening before stable strength is reached (Lohrmann et al., 2003). As described by Krantz (1991), the physical handling technique affects the friction coefficient and the density of sand. Poured sand is less densely packed and thus has different mechanical properties than sifted sand. If our sand is poured, its density is 1591 kg/m^3, whereas that of the sifted sand is 1681 kg/m^3. The poured sand has a friction angle of 30° and a cohesion of 80 Pa at peak friction. The friction angle reduces to 26° at stable friction (slight softening). The peak friction angle for sifted sand is considerably higher with 39° and a cohesion of 60 Pa. The stable friction angle of 27° is approximately identical with that of poured sand which is consistent with the results of Lohrmann et al. (2003). Note that the cohesion values cannot be determined accurately with our method and are probably subject to an error of about 30% (Lohrmann et al., 2003). Since the normal stress in our sand experiments is on the order of 320 Pa – about four times higher than the cohesion – we regard the critical shear stress as mainly friction-controlled (Lohrmann et al., 2003). The error on the friction angles is less than 1°.

Previous experiments using sand and clay with a setup similar to ours (e.g., Cloos, 1928; Riedel, 1929; Tchalenko, 1970;

Naylor et al., 1986) showed that the main shear zone above the basal velocity discontinuity usually evolves by interlinkage of smaller Riedel-, P-, and Y-shears into a complex anastomozing deformation zone. Such a complex pattern with a considerable vertical strain component would be too complex to be analyzed with the simple methods used here. However, we found a way to reduce the size of this anastomozing shear zone pattern to a scale below the resolution of our PIV vector determination and hence simply integrate over it. Shear zones evolving in our sand form a shear zone that is straight and parallel to the imposed basal velocity at the scale of observation, if we pour the sand into the box instead of sifting it. Within a 2–5 mm wide zone in the centre of this larger shear zone (with a width of ca. 6 cm, see Fig. 10), we observed low-angle Riedel shears as predicted by previous studies. They caused topographical differences on the order of 1 mm which we regard as negligible with respect to the imposed maximum horizontal displacement. The scale reduction of the Riedel shears is likely caused by the lower peak strength of the poured sand and the fact that it is undercompacted (Krantz, 1991; Lohrmann et al., 2003). Lower peak strength leads to smaller stress build-ups while compaction accommodates some additional strain. The progressive rotation of the micro-Riedel shears, the nucleation of new ones, and local compaction and decompaction cause slight fluctuations of the width of the central Riedel zone and with it of the larger master shear zone (on the order of 3 mm). These fluctuations and the fact that we interpolate over the micro-Riedel shears due to resolution limits explain the observed higher errors in the sand data (see Table 1). Sometimes, a larger single pop-up structure bounded by Riedel shears of 5 cm length, 2 cm width, and 0.5 cm height occurred very close to either the rear or front wall (in x-direction) of the shear box. But the remaining 25 cm of the shear zone remained undisturbed by structures of that scale and hence were suitable for this analysis.

6. Results

6.1. Newtonian material (PDMS)

Incremental and cumulative results show a coherent evolution (Figs. 7A,B, and 11A). Both widths, W' and W, remain constant after an initial growth period ($W = 15.7$ cm, $W' = 5.4$ cm). I_{loc} has a constant value of 0.7 for both the incremental and cumulative history. This is because the strain rate distribution remains constant due to strain independence of viscosity, which matches the expectations for a Newtonian material. Incremental Exy_{mean}, Exy_{max}, and displacement remain constant over the duration of the experiment (Fig. 7C). Data scattering is due to correlation noise which is only visible at the scale of the small incremental values. However, the cumulative plots exhibit well-correlated linear functions (Fig. 7D) implying constant mean and maximum shear strain rates as well as displacement rate, which again reflect the strain independence of this material.

Total finite displacement is 4.72 cm which is 94.5% of the imposed 5 cm bulk displacement. This observation holds for the other materials as well (Carbopol: 4.72 cm, P80PL20: 4.82 cm, Sand: 5.01 cm, Figs. 8D, 9D, and 10D). This means our total width determination criterion is reasonable. Deviations from total bulk displacement reflect PIV measurement errors (Table 1, Appendix) and strain reversals due to corner flow close to the box boundaries.

6.2. Strain-hardening material (P80PL20)

The temporal evolution of incremental and cumulative data (Figs. 8A,B, and 11B) is in overall agreement. The total width W increases during the first half of the experiment from 14.8 to 16.4 cm (ca. 11%). Width W' at 1/3 of Exy_{max} increases constantly from 5.4 to 6.3 cm for the incremental data (16.7%), and from 5.4 to 5.8 cm for the cumulative data (7.4%). Incremental I_{loc} appears to decrease slightly from 0.70 to 0.68 (ca. −3%). The cumulative data display even less change in I_{loc}. It apparently grows from 0.703 to 0.707 for the first half of the experiment and finally reduces continuously to 0.699. Hence, changes of I_{loc} lie well within the range of measurement errors (see Appendix). However, the incremental evolution of shear strains shows that Exy_{max} decreases over time whereas Exy_{mean} remains constant after an initial step-like drop (4800 s, Fig. 8C). This implies a decrease in I_{loc}. Incremental displacement is approximately constant, which can also be seen in the linear displacement–time function in the cumulative data. Cumulative Exy_{max} exhibits a slightly non-linear relation with time indicating a small decrease in maximum shear strain rate (Fig. 8D). Mean shear strain rate decreases after 8400 s. This behaviour is an expression of strain hardening of the material which deforms in its non-linear domain due to the low bulk strain rate employed in the experiment (Boutelier et al., in press). In summary, the predicted shear zone behaviour for a strain-hardening material, i.e., progressive widening (Means, 1984, 1995; Hull, 1988), decrease in maximum shear strain rate, and (little) delocalization, is confirmed by this experiment.

6.3. Strain-softening material (Carbopol)

This pseudoplastic material shows the expected differences in incremental and cumulative history (Figs. 9A,B, and 11C). Incremental W drops after the material yields (at 2160 s) from initially 9.2 to ca. 6.4 cm (−30%) and stays approximately constant thereafter. Incremental W' exhibits similar behaviour, decreasing from 6.9 cm to a constant value of 3.6 cm after yielding (−48%). Cumulative W grows from 10.2 cm in the initiation period to 12.4 cm at yield and then progressively decreases to 10.7 cm (−14%). Cumulative W' evolution resembles the incremental W' history, decreasing from 6.6 cm at yield to about 4.2 cm (after 5760 s) with continuous minor diminution to a final value of 3.8 cm (total −42%). Incremental I_{loc} increases from 0.38 to 0.51 at yield and subsequently reaches a constant value of 0.53 (+39%). Cumulative I_{loc} grows from 0.48 to 0.55 at yield and increases non-linearly to an approximately constant value of 0.71 (8640 s, total +48%)

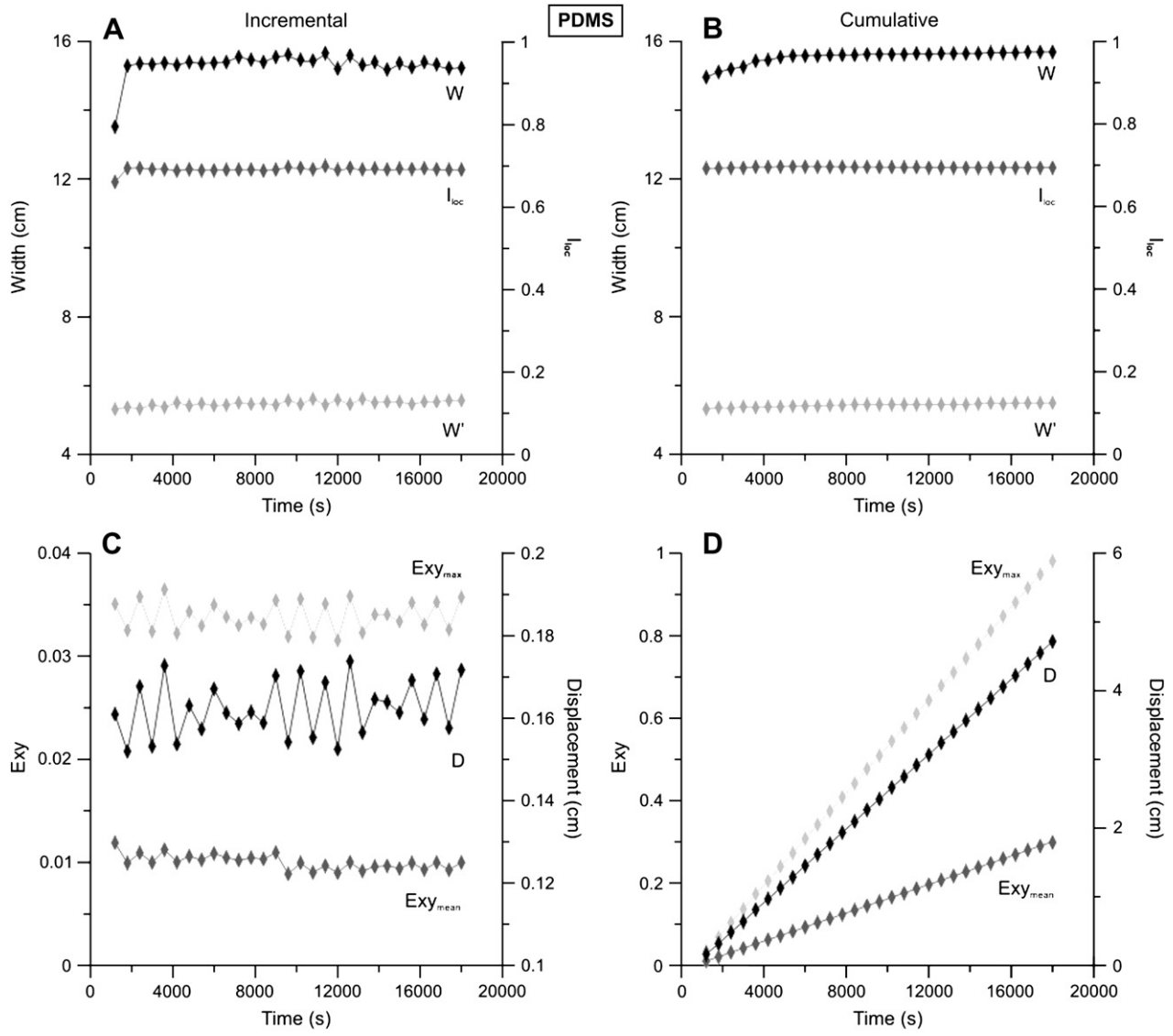

Fig. 7. Incremental and cumulative results for Newtonian material (PDMS) experiment. Incremental [A] and cumulative [B] evolution of W, W', and I_{loc} over time. Incremental [C] and cumulative [D] evolution of Exy_{max}, Exy_{mean}, and D over time. See text for further explanation.

afterwards. The effects of the strain softening caused by the pseudoplastic yield point of Carbopol are also clearly visible in the incremental strain plots (Fig. 9C). Mean and maximum shear strain increase to constant values within two time steps after yielding. Note that the yield point occurs at a critical strain of 2%, as predicted by the rheometer results, and is best illustrated by the mean strain (Fig. 9C). The relative increase of Exy_{max} is larger than that of Exy_{mean} causing the observed growth in I_{loc}. The significant increase in maximum shear strain rate after yield is also clearly depicted in the cumulative strain plot (Fig. 9D). The predicted shear zone behaviour for softening materials is confirmed in this experiment: narrowing of the actively deforming shear zone centre (as displayed in the incremental width plot; Means, 1984, 1995; Hull, 1988), increasing maximum shear strain rate, as well as increasing finite I_{loc} (cumulative data, Schrank et al., in press). The cumulative width decreases for a longer period of time than the incremental width. This is because the shoulders of the finite shear strain profiles remain elevated due to the small strains localized at the margins of the initially more distributed shear zone before yield (Fig. 1B). Hence, finite data display apparent narrowing in their later stages leading to an overestimation of the actually active shear zone width.

6.4. Mohr–Coulomb material

The incremental and cumulative data for poured quartz sand show a similar evolution in terms of width but exhibit interesting differences in the evolution of I_{loc} (Figs. 10A,B, and 11D). Incremental I_{loc} and W show four obvious outliers. These are related to errors of the strain interpolation. The small-scale width fluctuations due to Riedel shears mentioned above generated a small strain increase at the left boundary of

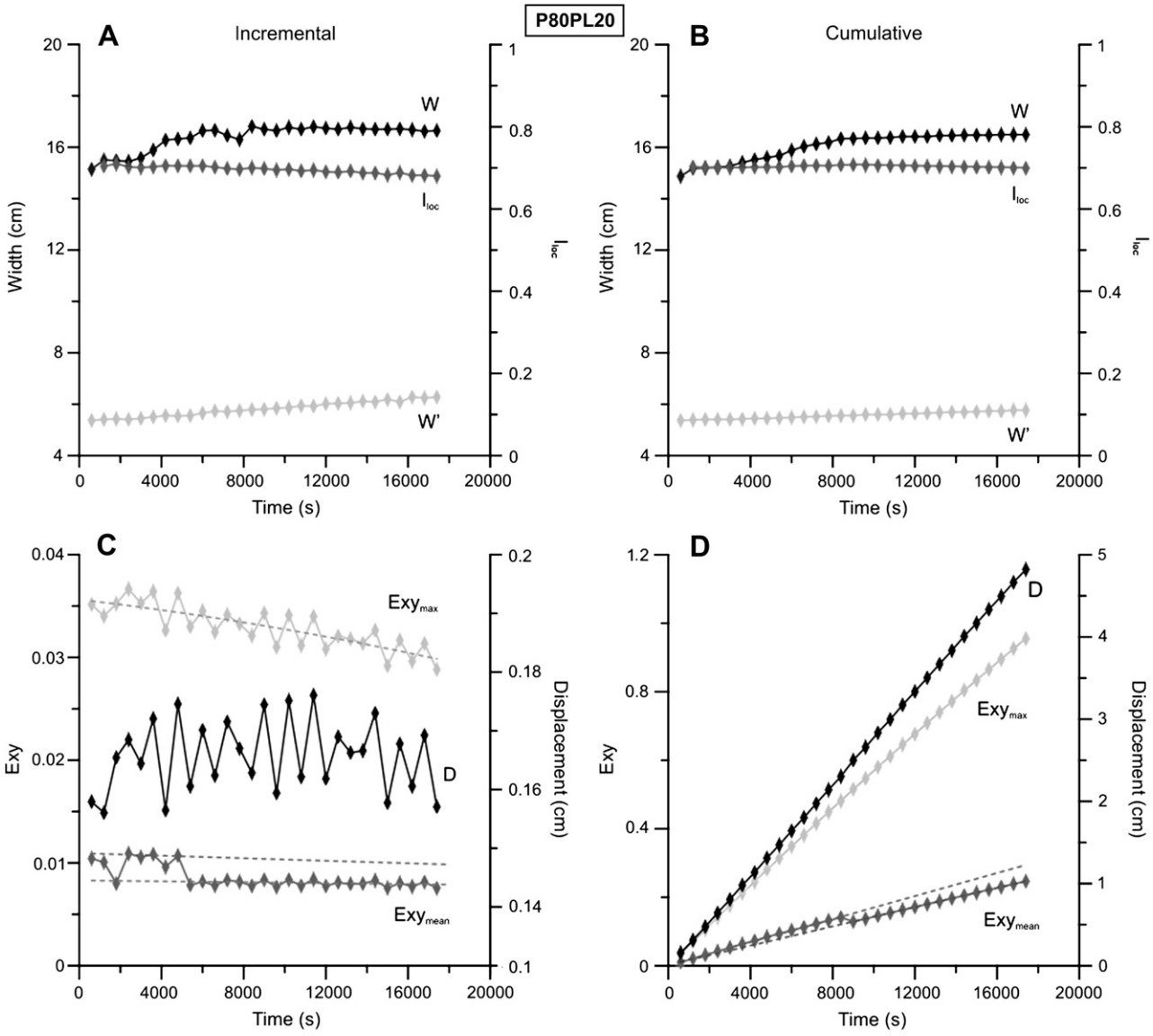

Fig. 8. Results for shear zone experiments with strain-hardening material P80PL20. Incremental [A] and cumulative [B] evolution of W, W', and I_{loc} over time. Incremental [C] and cumulative [D] evolution of Exy_{max}, Exy_{mean}, and D over time. Dashed lines in [C] and [D] are linear least-square interpolations emphasizing changes in curve gradients. See text for further explanation.

the central strain profile such that interpolation over it caused a slight tilting of the shoulder of the strain profile resulting in an artificial, very small non-zero strain gradient over a few centimetres. This underlines a typical noise problem in our automated zero-gradient method for the determination of shear zone width. Hence, we recommend to always visually check the strain profiles with the calculated boundaries. However, ignoring the extreme outliers, incremental W reduces from an initial value of 8.8 cm to an approximately constant value of 5.7 cm after 1080 s (ca. −35%). Incremental W' decreases from 3.3 cm to a constant value of 2.7 cm after 1800 s (−18%). Incremental I_{loc} decreases from about 0.69 during the first two time steps to a constant value of 0.61. Cumulative W decreases from 8.8 cm to an approximately constant value of 5.7 cm (−35%) after 6840 s whereas W' decreases from 3.3 cm to a constant value of 2.7 cm (−18%) after 7200 s. Interestingly, cumulative I_{loc} decreases from an initial value of about 0.69 for the first 2520 s of the experiment to a constant value of 0.61 after 6480 s. Incremental Exy_{max} fluctuates around a mean value of 0.08 after 720 s (Fig. 10C). Incremental Exy_{mean} exhibits similar behaviour, saturating at a constant value of 0.03. The cumulative Exy_{max} and displacement curves (Fig. 10D) display little deviation from linearity, implying constant maximum strain and displacement rates. The Exy_{mean} curve appears to be slightly concave upwards which indicates an increase in mean strain rate. If one interpolates the Exy_{mean} curve linearly for the data points until the major drop in cumulative width occurs, one obtains a mean strain rate of $6.5 \times 10^{-5}\ s^{-1}$ whereas an interpolation for the rest of the data yields $9.5 \times 10^{-5}\ s^{-1}$. This is because the constant displacement rate must be accommodated within a narrower shear zone after about 3000 s. The latter cumulative mean

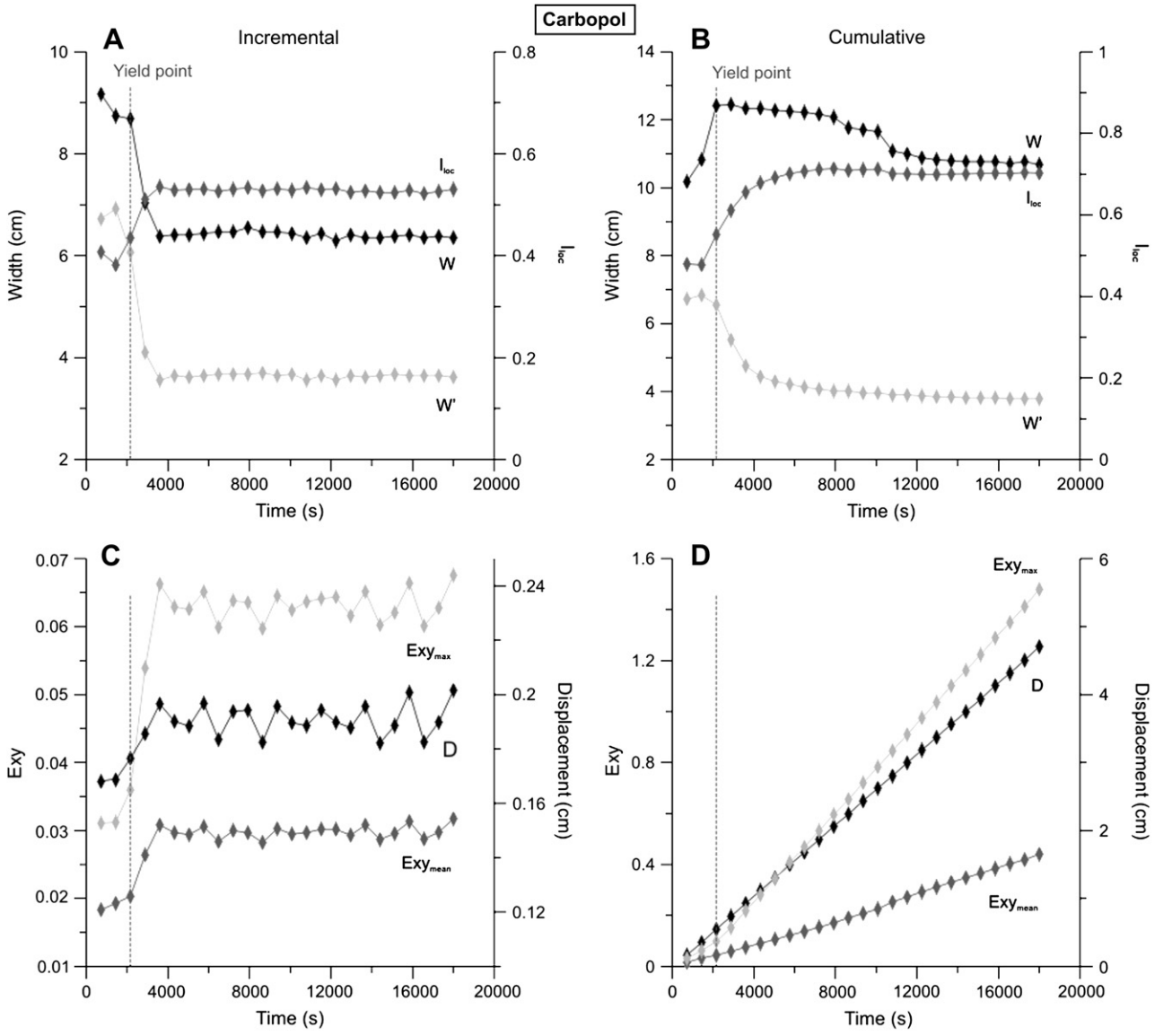

Fig. 9. Results of shear zone experiment with strongly strain-softening material (Carbopol). Incremental [A] and cumulative [B] evolution of W, W', and I_{loc} over time. Incremental [C] and cumulative [D] evolution of Exy_{max}, Exy_{mean}, and D over time. Dashed line marks yield point followed by rapid strain softening. Yielding coincides with 2% incremental mean strain in [C] as predicted by rheological measurements (Fig. 5). See text for further discussion.

strain rate is consistent with the averaged incremental mean strain rate of $8.7 \times 10^{-5}\ s^{-1}$ for the same experimental stage. These observations explain the unexpected decrease in I_{loc}. The poured sand exhibits a small decrease in friction angle from 30° to 26°. Hence, this material is expected to be slightly strain softening. We observe the expected reduction in cumulative shear zone width but I_{loc} decreases as well. This is because – as opposed to the strongly softening material Carbopol – the maximum strain rate remains constant while the shear zone narrows in the cumulative data. This consequently leads to an increase in cumulative mean strain rate and a less localized cumulative strain distribution within the shear zone. The incremental width curve (Fig. 10A) shows that the shear zone quickly attains a constant small width. Careful observation of the experiment revealed that the initial two time steps of the experiment capture a period of rather distributed strain before full localized failure along the entire length of the box occurs. Once the complete fault zone is established, its incremental width and the maximum strain rate remain constant. It follows that the poured sand does not behave like a softening material but rather like an almost perfectly plastic material, at least for the normal stresses in our experiment. The apparent prolonged narrowing of width displayed in the cumulative data is due to the effects explained in the previous section on Carbopol.

7. Influence of boundary conditions

In order to understand the effect of the no-slip boundary condition on shear strain distribution, we performed experiments with a variety of filling heights of PDMS (i.e., 1 and 3.5 cm as opposed to 2 cm) and an experiment with a 1 cm thick layer of PDMS that was decoupled from the base of the box by a 2 cm layer of low-viscosity (ca. 100 Pa s) corn

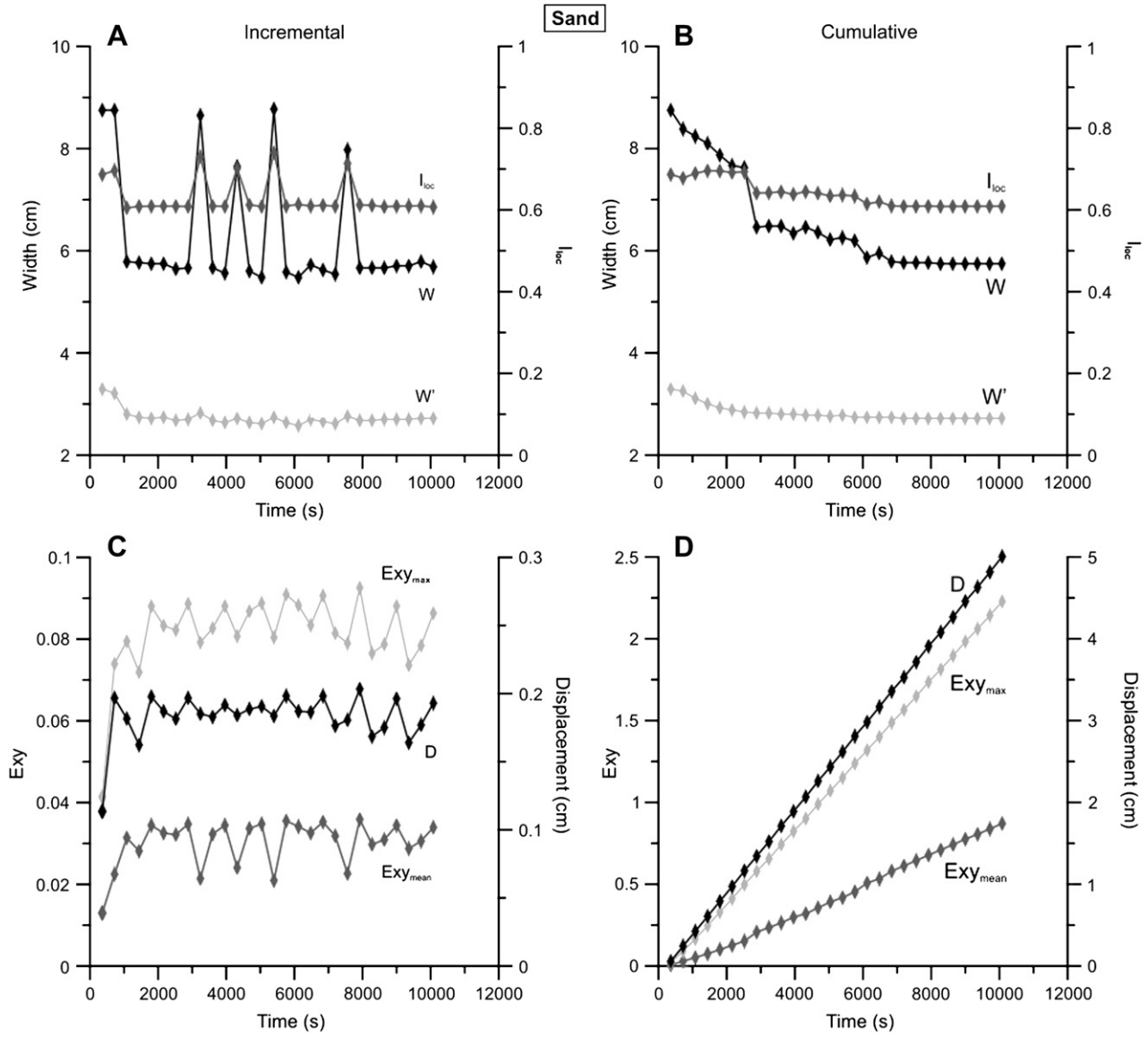

Fig. 10. Results of shear zone experiment with weakly strain-softening material (quartz sand). Incremental [A] and cumulative [B] evolution of W, W', and I_{loc} over time. Incremental [C] and cumulative [D] evolution of Exy_{max}, Exy_{mean}, and D over time. See text for discussion.

syrup (Fig. 12A). We used PDMS for all these experiments because of its simple, strain-independent rheology.

The effect of kinematic boundary conditions is profound. For a thin 1 cm non-decoupled layer of PDMS we find a highly localized shear strain profile. Shear strain distribution becomes systematically less heterogeneous with increasing layer thickness due to the increasing distance of the free surface to the box bottom. We used these data to derive a hypothetical shear zone boundary in the *yz*-plane for a 4 cm layer that underlines the importance of the basal no-slip condition (Fig. 12B). The decoupled layer exhibits an approximately parabolic strain profile displaying no localization within the shear zone (Fig. 12A, I_{loc} is 0.31 for this profile). Thus, driving shear from the bottom (i.e., by the no-slip kinematic boundary condition at box base) along a sharp velocity discontinuity causes kinematically imposed localized strain patterns even in Newtonian (i.e., non-localizing) materials.

8. Discussion: limitations and challenges in determining rheology from natural shear zones

Our experiments confirm some common predictions concerning shear zone behaviour as a function of material properties, namely in terms of widening/narrowing with time and evolution of transversal strain distribution: (1) Newtonian materials (PDMS) exhibit no relevant change of shear zone width or strain distribution due to the strain independence of material properties. (2) Strain-hardening materials (P80PL20) undergo successive shear zone widening and delocalization of the shear strain distribution (decrease in I_{loc}). The latter effect was subtle in the experiment presented here due to rather weak hardening of the employed analogue material. The results of Boutelier et al. (in press) imply that the viscosity increase for this material over the range of our experimental strains is smaller than a factor of 5. Materials with more pronounced

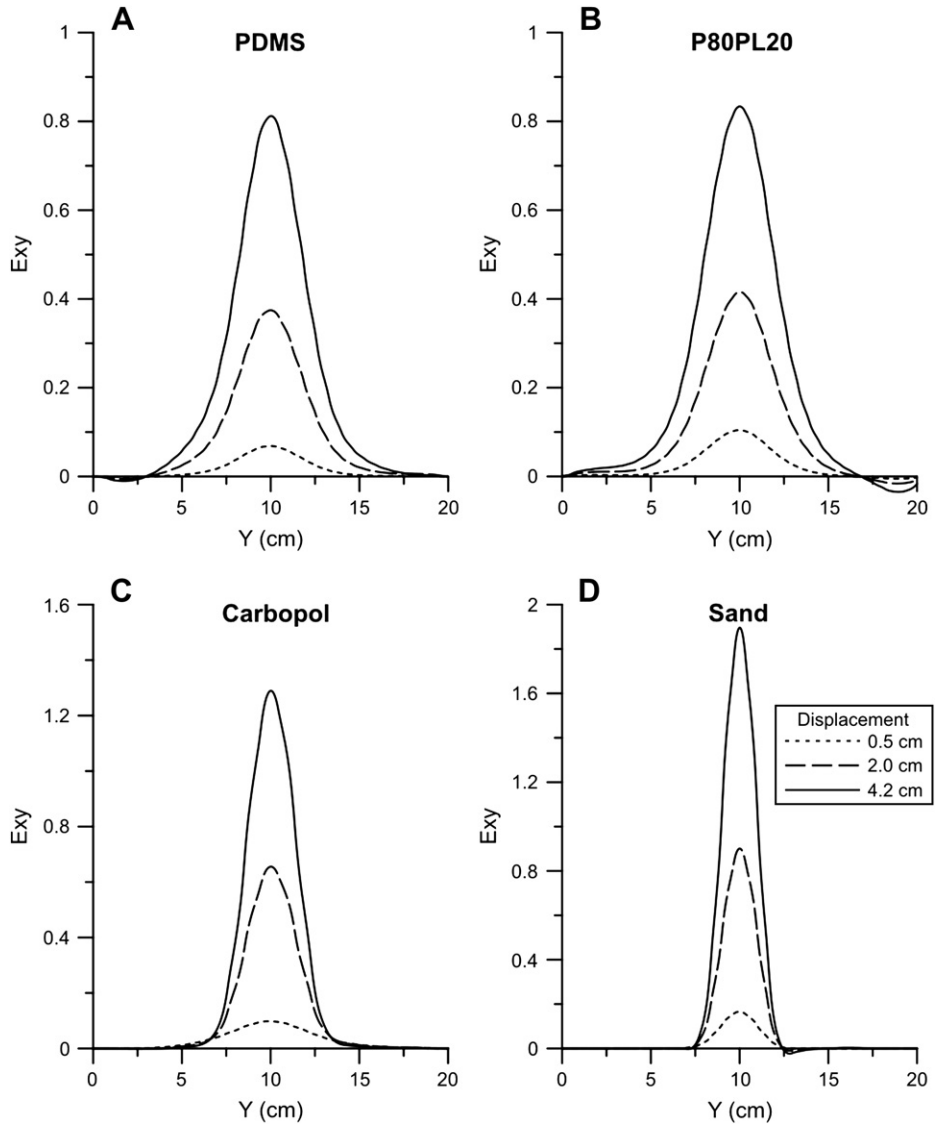

Fig. 11. Cumulative strain profiles at different experimental stages for the materials presented in this study: [A] PDMS, [B] P80PL20, [C] Carbopol, and [D] poured sand.

strain hardening are expected to display stronger delocalization. Larger finite shear strains are common in nature and may also increase the delocalization effect. (3) Strongly strain-softening materials develop narrowing shear zones and exhibit a progressive increase of localization intensity I_{loc} after yielding (Carbopol). The maximum strain rate in Carbopol increases by about factor 2 after yield. In shear experiments on natural rocks, Holyoke and Tullis (2006) determined an increase of shear strain rate of about one order of magnitude after failure (comparing bulk strain rate before failure to strain rate in the failed shear zone). We therefore suggest that the relative weakening of Carbopol does not exceed that of some natural shear zones. In addition, we found that both I_{loc} and width decrease in poured sand. We argue that this occurs because the poured sand behaves like an almost perfectly plastic material with only minor softening, if at all. The maximum shear strain rate in this sand remains constant whereas it increases for materials that soften significantly after yield. This observation demonstrates that the strain localization intensity does not only decrease in hardening materials. Hence, a decrease in I_{loc} alone is not an unambiguous indicator of a strain-hardening rheology (given all the simplified assumptions of our experimental setup). However, if I_{loc} and the width evolution are considered together, it seems possible to differentiate certain rheological end member materials qualitatively. The I_{loc} and width evolution represent different strategies to recognise softening/hardening behaviour in shear zones. By regarding shear zone width evolution, one is essentially looking at localization at a scale larger than that of the shear zone itself. In contrast, the evolution of the strain distribution (I_{loc}) represents a dimensionless perspective from within the shear zone. Both approaches have advantages and problems that will be discussed further below.

Our experimental results imply that qualitative information on rheology may be derived from natural shear zones, given the assumptions of a continuous deformational event in

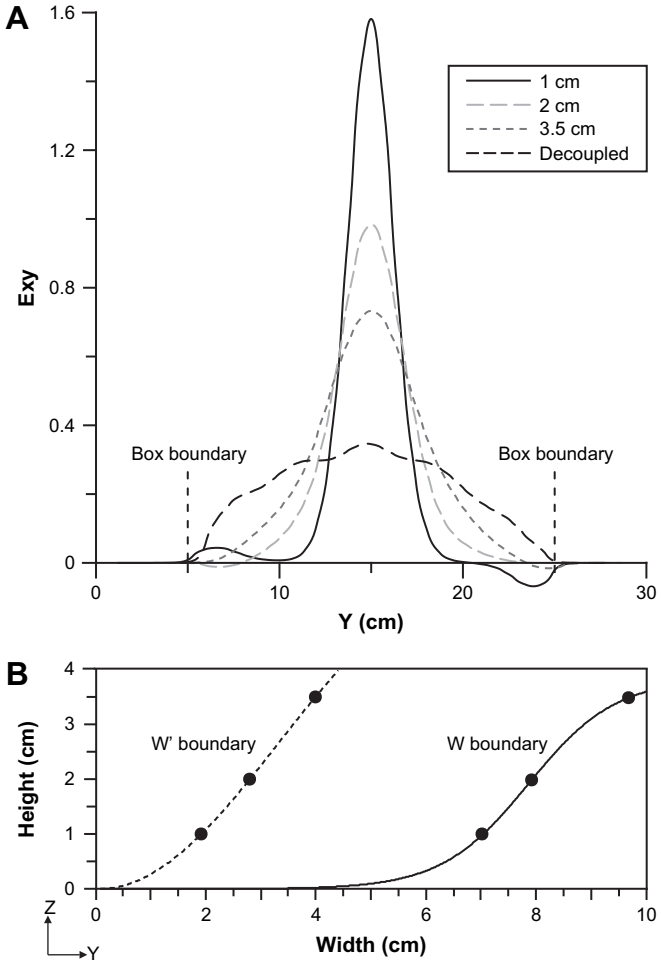

Fig. 12. Influence of kinematic boundary conditions. [A] Finite shear strain profiles after 5 cm total displacement for four different PDMS experiments. The Gaussian curves represent experiments with different layer thicknesses of PDMS. The parabolic curve (dashed line labeled "Decoupled" in legend) represents an experiment where a 1 cm PDMS layer was decoupled from the box bottom by a 2 cm layer of low-viscosity (ca. 100 Pa s) corn syrup. [B] Hypothetical shear zone boundary in vertical cross section normal to x for box entirely filled with PDMS. Note that only one half of the box is shown. The velocity discontinuity is at the origin of the coordinate system. Solid line denotes total width W, dashed line displays W'.

isotropic materials under constant bulk displacement conditions without changes in kinematics, temperature, deformation mechanism, and composition as well as the availability of temporally well-constrained data. How might this be accomplished practically in the field? Even if the former, oversimplified conditions could be established in nature, the problem of sufficient time constraints prevails (e.g., Means, 1995). Absolute age dating methods are generally insufficient in terms of resolution or too intricate to be applied to a statistically significant number of shear zones. A common, but still difficult, way around this dilemma is to use space as a proxy for time (e.g., Mitra, 1979, 1984; Means, 1995; Fusseis et al., 2006; Holyoke and Tullis, 2006). This strategy is applied to either a single shear zone, assuming that the shear zone propagates longitudinally/laterally and hence preserves younger fabrics at the tips/margins than in its centre, or it is applied to a set of shear zones assuming that larger shear zones accommodating greater displacements are older than smaller ones. Both strategies share a common disadvantage: space as a proxy for time is unlikely to scale linearly with time. In other words, equidistant space intervals most likely do not represent equal time intervals. Hence, comparability to quantitative, time-controlled experimental data will always be qualitative. In the following section, we discuss problems of width and I_{loc} determination for both single- and multi-shear zone strategies, followed by remarks on quantitative rheological estimates using analytical and numerical methods.

8.1. Common measurement uncertainties

Intrinsic measurements errors relevant to both width and strain distribution determination are unavoidable. Complete 3D exposures of shear zones are rarely observed in the field. Even if an assumption of plane-strain deformation is valid, deviations of 2D outcrop surfaces from the xz-plane of the strain ellipsoid are common and lead to either underestimation or overestimation of shear zone width (for a more detailed discussion of width, length, and area measurement bias, see Schrank et al., in press). Shear zone width and strain distribution are typically determined by comparing marker deflections to an unsheared (or homogeneously sheared) initial marker orientation in the host rock (Ramsay and Graham, 1970). If the initial marker orientation is not homogeneous (e.g., the global foliation orientation fluctuates by $\pm 5^{\circ}$, which is common in the field), additional errors arise. Moreover, local lithological heterogeneities at a scale comparable to that of the shear zone itself significantly affect both the strain distribution and width along a single shear zone due to their differing mechanical properties (e.g., Schrank et al., in press). Our experiments showed that the active shear zone width in strain softening shear zones is generally overestimated from finite strain profiles. This is because initial localization at the later deactivated low-strain margins is difficult to differentiate from deformation in the later active central portion. This effect should be more pronounced in heterogeneous natural materials where strain determination is more prone to noise. A relevant additional bias for I_{loc} is caused by uncertainties in maximum shear strain determination that increase with shear strain (Ramsay and Graham, 1970). Note that the contribution of the width determination error to the total error of I_{loc} is minor (see Eqs. (3), (4), and (7)). The contribution of displacement uncertainties can be minimized if appropriate passive markers exist.

8.2. Problems in single shear zone strategy

If we want to study a spatial sequence of strain profiles or widths on a single shear zone, we must consider data along (i.e., in longitudinal direction) the shear zone, assuming that its tip is younger than its centre. Shear zone tips are likely inappropriate locations for characterizing either width or I_{loc} from a 2D section because they deviate significantly from plane strain, simple shear conditions (Coward, 1976; Ramsay,

1980; Simpson, 1983). Hence, the shear zone tip should be disregarded in such analyses. However, it will be difficult to decide in the field at exactly which distance from the tip we should measure width and strain distribution. Additionally, our experiments showed that the model shear zones reach a steady state at higher strains, after which the parameters of interest do not change. This implies that major characteristic changes in localization geometry related to material properties might often occur at transient low-strain stages that should be preserved quite close to the tips of natural shear zones, rather than in their centres. Moreover, the total bulk mean strain in our experiments is low compared to strains accommodated in natural shear zones. Thus, the segment of interest preserving these early relevant localization stages might be small in natural shear zones. However, the ratio of our hardening/softening rates versus experimental bulk strain rate is not scaled with respect to natural rates. If hardening and softening rates of natural materials are significantly lower compared to bulk strain rate, this problem is less acute.

Considering the above discussion, we recommend investigating meso- to large-scale (>10 m long) shear zones along their strike. Small-scale shear zones represent low-strain stages of localization. Due to their small length, boundary effects of the tips are likely to interfere with the entire shear zone, which then strongly deviates from plane-strain simple shear (cf. Coward, 1976). However, our experiments showed that at least material-related responses such as widening/narrowing can be observed in the centres of such low-aspect ratio low-strain shear zones. Since our model shear zones do not display significant width changes along strike due to the kinematic boundary conditions (Fig. 3B), temporal control of one given transversal profile is sufficient, which is hardly possible in nature. Large natural ductile shear zones incorporate mylonitic fabrics in their centres (e.g., White et al., 1980; Carreras and Casas, 1987; Carreras, 2001,). This facilitates the identification of domains suitable for strain distribution and width considerations. As shown above, careful studies of width and I_{loc} in concert might reveal useful qualitative rheological information. Schrank et al. (in press) present a plot of I_{loc} versus distance from the shear zone tip for a 16-m section of a mylonitic shear zone whose termination exhibits coeval brittle and viscous deformation mechanisms (Fusseis et al., 2006). The first mylonite in the centre of this shear zone occurs about 3.5 m away from the brittle–ductile shear zone termination. I_{loc} clearly increases over the entire section from ca. 0.63 to 0.95 (Fig. 13A) acquiring most of its increase along the mylonitic part. Softening was also inferred independently (Fusseis et al., 2006). This strong increase resembles the behaviour of our strongly softening material (Fig. 13). However, we must take into account that the regarded natural shear zone developed in anisotropic rocks (Carreras, 2001) under conditions that were not as simple as those in our experiments. Restrictions of the space-for-time substitution apply as well (see above). The resemblance of the graphs is hence strictly qualitative.

8.3. Problems in multi-shear zone strategy

The main problem in considering multiple shear zones as space-for-time proxies is related to the fact that it is likely that shear zones of significantly different length scales will be regarded. Simple width statistics will not constrain narrowing/widening and the related rheology because a shear zone of 1 m length will always be thinner than a shear zone of 1 km length. Moreover, for scale changes over orders of magnitude, rheology is scale-dependent (e.g., Schrank et al., in press). In contrast, I_{loc} may be a more suitable tool for the analysis of multiscale data sets, because it is a dimensionless measure of strain distribution independent of scale. Schrank et al. (in press) observed a systematic increase of I_{loc} with length and width for mm- to dm-scale shear bands. However, their data scatter is large and additional investigations are required. In

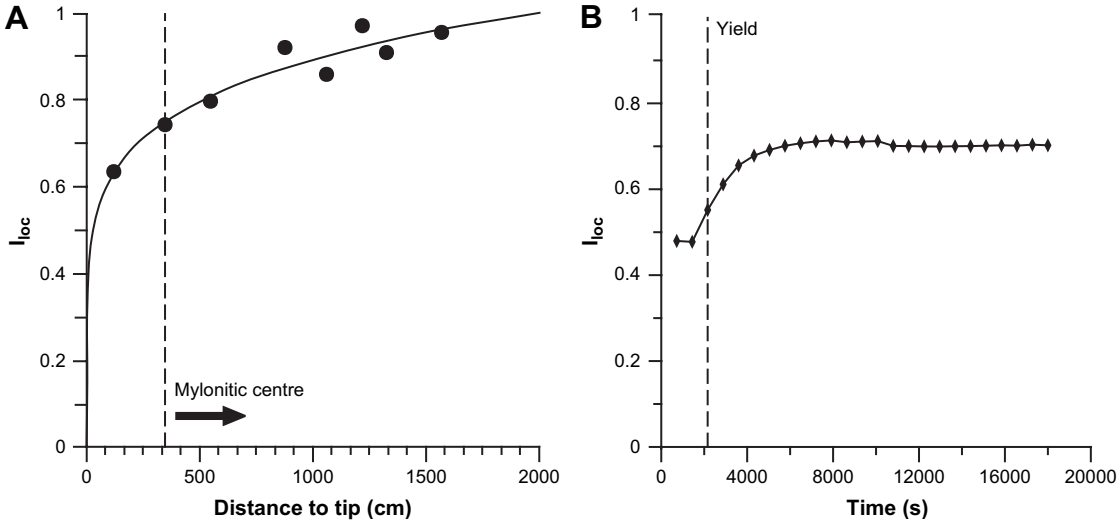

Fig. 13. [A] Plot of I_{loc} versus distance from shear zone tip for an m-scale mylonitic shear zone (modified from Schrank et al., in press. See also Fig. 5 in Fusseis et al., 2006). Dashed line denotes presence of mylonite in shear zone centre. [B] Temporal evolution of finite I_{loc} for strongly softening material (Carbopol, see also Fig. 9).

addition, we have shown above that I_{loc} alone yields ambiguous results for hardening and plastic, non-softening rheologies (P80Pl20 versus poured sand). Yet, a clear increase in cumulative I_{loc} seems to be a reliable indicator for softening materials.

8.4. Challenges in quantitative rheological estimates from shear zones with analytical and numerical methods

Deriving quantitative rheological estimates from natural shear zone geometries is challenging. Our experiments illustrate the profound effect of kinematic boundary conditions on shear strain distributions. Given zero slip at the bottom of the shear box, even Newtonian PDMS resembles a localizing material in terms of finite shear strain distribution. Any 2D consideration of this experiment would be misleading because localization is forced by the kinematic boundary conditions, as opposed to strain dependence of the material. This does not apply to the qualitative validity of our standard experiments since we determined the temporal evolution of shear zone width as well as strain distribution as a function of known material properties assuming that localization had occurred. However, nature essentially produces heterogeneous 3D deformation for some boundary conditions (e.g., Jiang and White, 1995) that must be accounted for when deriving quantitative rheological measures from finite structures on any given scale. Shear zones that do not reach Earth's surface are entirely laterally confined; hence 3D no-slip boundary conditions should apply in general for small- to mesoscale structures.

9. Conclusions

Our experiments confirmed that shear zones in strain-hardening materials widen with time while their transversal strain distribution becomes less heterogeneous, whereas shear zones in strain-softening materials narrow progressively with an increasingly localized strain distribution. In contrast, shear zones in plastic, non-softening materials display shear zone narrowing with decreasing localization intensity. These effects are observed in the finite data of our model shear zones and hence might be recognizable in natural finite shear zones.

The determination of qualitative rheological estimates from finite geometrical shear zone parameters in nature is challenging despite the encouraging results of our laboratory models. Successful attempts should include a combination of both statistically significant width and I_{loc} measurements at meso- to large scales as well as additional independent field constraints. Simple width analysis should not be used for multiscale data sets whereas I_{loc} might be a suitable tool to, at least, identify softening rheologies. Further constraints on how strain is accommodated in shear zone terminations might help to improve our understanding of early stages of localization and how they relate to the rheology of deforming rocks. A thorough understanding of boundary conditions is paramount for the quantitative rheological interpretation of natural data. 3D multiscale numerical or physical experiments as well as analytical considerations that carefully investigate various possible natural boundary conditions (e.g., large-scale end members such as crustal-scale thrust/normal faults versus strike-slip faults or entirely laterally confined shear zones with a given rheology) should be employed to develop quantitative tools for assessing the relation between rheology and shear zone geometry in the field.

Acknowledgements

Amelia Bain and Viktoria Georgieva are thanked for conducting shear zone experiments and rheological measurements during their research internships in our laboratory. Reviews by J. Carreras, C. Talbot and J. Urai helped to improve and clarify the manuscript. Funding was provided by the University of Toronto and a Natural Sciences and Engineering Council of Canada Discovery Grant to ARC.

Appendix

The derivation of errors for the PIV measurements is complex in detail. Errors arise from two main sources (Huang et al., 1997, and references therein): the experimental setup and conditions as well as the particle-displacement detection algorithms used. Experimental errors are related to the size and density distribution of the displacement markers, the illumination uniformity, the ratio of image recording frequency to displacement rate, camera resolution, etc. Some of the error sources may vary within one image (e.g., marker particle density) and over the duration of an experiment (e.g., illumination). However, they can be determined empirically for each image. Errors arising from the displacement detection algorithm are for example related to the choice of search window size and overlap as well as the peak location method. However, the derivation of the related equations as well as an exact error estimation for each data point are too intricate and beyond the scope of this paper. Instead, we present an empirical error analysis.

The image recording frequency of the PIV cameras is very accurate (on the order of microseconds). Hence, we can determine the imposed displacement rate from the recorded images for each experiment with high precision (Table 1). This was done to minimize rate errors due to rounding errors introduced by the stepper motor. For the cumulative data, the observed displacement rate in the shear zone was determined from the slope of the displacement–time curves (Figs. 7–10) and compared to the imposed displacement rate. The imposed and observed displacement per time step (as defined by the time interval between two images) could be calculated easily and with it the observed absolute displacement error (between 0.07 and 0.001 mm, Table 1).

For the incremental data, the observed displacement rate was calculated as the mean of the displacement–time curves. The standard deviation of this mean displacement rate and its deviation from the imposed rate are both given in Table 1. Data scatter is higher for the incremental data because the

signal-to-noise ratio is smaller than for the cumulative data. Hence, we determined the maximum observed displacement deviation with respect to the imposed displacement per time step and defined it as the maximum absolute displacement error (between 0.25 and 0.06 mm). This is a conservative error estimate. From both incremental and cumulative displacement errors, the resulting strain errors were approximated with an empirical relation taking search window size and overlap into account (LaVision, 2005).

The errors for all other measures considered, i.e., shear zone width and I_{loc}, could be calculated analytically. Since the width determination error would require a mathematical description of each strain profile (compare Section 4 for measurement details), we decided to estimate this error empirically with a very conservative estimate of ±1 cm. The absolute error of I_{loc}, $u_{I_{loc}}$, assuming linear error propagation is:

$$u_{I_{loc}} = \left|\frac{D}{W^2 \mathrm{Exy}_{max}}\right| u_W + \left|\frac{1}{W \mathrm{Exy}_{max}}\right| u_D + \left|\frac{D}{W(\mathrm{Exy}_{max})^2}\right| u_{\mathrm{Exy}_{max}} \quad (7)$$

D is displacement, W denotes shear zone width, Exy_{max} is maximum shear strain, u_D is displacement error, and $u_{\mathrm{Exy}_{max}}$ is maximum shear strain error. See Section 4 for definitions. The strain determination error is the most significant error source (see also discussion in appendix of Fusseis et al., 2006). The absolute error of I_{loc} ranges from ±0.15 for small strains/displacements in the beginning of the experiments and for the incremental data reducing to ±0.02 at steady state in the cumulative data.

References

Abbassi, M.R., Mancktelow, N.S., 1992. Single layer buckle folding in non-linear materials: I. Experimental study of fold development from an isolated initial perturbation. Journal of Structural Geology 14, 85–104.

Adam, J., Urai, J.L., Wieneke, B., Oncken, O., Pfeiffer, K., Kukowski, N., Lohrmann, J., Hoth, S., van der Zee, W., Schmatz, J., 2005. Shear localisation and strain distribution during tectonic faulting – new insights from granular-flow experiments and high-resolution optical image correlation techniques. Journal of Structural Geology 27, 283–301.

Bayly, M.B., 1970. Viscosity and anisotropy estimates from measurements on chevron folds. Tectonophysics 9, 459–474.

Biot, M.A., 1957. Folding instability of a layered viscoelastic medium under compression. Proceedings of the Royal Society of London, Series A: Mathematical and Physical Sciences, 444–454.

Biot, M.A., 1961. Theory of folding of stratified viscoelastic media and its implications in tectonics and orogenesis. Geological Society of America Bulletin 72 (11), 1595–1620.

Biot, M.A., Ode, H., Roever, W.L., 1961. Experimental verification of the theory of folding of stratified viscoelastic media. Geological Society of America Bulletin 72 (11), 1621–1631.

Boutelier, D., Schrank, C., Cruden, A.R. Power-law viscous materials for analogue experiments: new data on the rheology of highly-filled silicone polymers. Journal of Structural Geology, in press. doi:10.1016/j.jsg.2007.10.009

Byerlee, J., 1978. Friction of rocks. Pure and Applied Geophysics 116, 615–626.

Carreras, J., Casas, J.M., 1987. On folding and shear zone-development: a mesoscale structural study on the transition between two different tectonic styles. Tectonophysics 135, 87–98.

Carreras, J., 2001. Zooming on Northern Cap de Creus shear zones. Journal of Structural Geology 23, 1457–1486.

Cloos, H., 1928. Experimente zur inneren Tektonik. Zentralblatt fuer Mineralogie, Geologie und Palaeontologie Abt. B, 609–621.

Cobbold, P.R., Cosgrove, J.W., Summers, M., 1971. The development of internal structures in deformed anisotropic rocks. Tectonophysics 12, 23–53.

Cobbold, P.R., Gapais, D., Rossello, E.A., 1991. Partitioning of transpressive motions within a sigmoidal foldbelt: the Variscan Sierras Australes, Argentina. Journal of Structural Geology 13, 743–758.

Cosgrove, J.W., 1989. Cleavage, folding and the finite strain ellipsoid. Proceedings of the Geologists' Association 100 (4), 461–479.

Coward, M.P., 1976. Strain within ductile shear zones. Tectonophysics 34, 181–197.

Evans, B., Kohlstedt, D.L., 1995. Rheology of rocks. In: Ahrens, T.J. (Ed.), Rock Physics and Phase Relations: a Handbook of Physical Constants. American Geophysical Union, Washington, pp. 148–165.

Fusseis, F., Handy, M.R., Schrank, C.E., 2006. Networking of shear zones at the brittle-to-viscous transition (Cap de Creus, NE Spain). Journal of Structural Geology 28, 1228–1243.

Garstecki, A., Glema, A., Lodygowski, T., 2003. Sensitivity of plastic strain localization zones to boundary and initial conditions. Computational Mechanics 30, 164–169, doi:10.1007/S00466-002-0376-1.

Grujic, D., Mancktelow, N.S., 1998. Melt-bearing shear zones: analogue experiments and comparison with examples from southern Madagascar. Journal of Structural Geology 20, 673–680.

Holyoke, C.W., Tullis, J., 2006. Formation and maintenance of shear zones. Geology 34 (2), 105–108.

Huang, H., Dabiri, D., Gharib, M., 1997. On errors of digital particle image velocimetry. Measurement Science and Technology 8, 1427–1440.

Hubbert, M.K., 1951. Mechanical basis for certain familiar geologic structures. Geological Society of America Bulletin 62, 355–372.

Hudleston, P.J., Lan, L., 1994. Rheological controls on the shape of single-layer folds. Journal of Structural Geology 16, 1007–1021.

Hull, J., 1988. Thickness–displacement relationships for deformation zones. Journal of Structural Geology 10, 431–435.

Jessell, M.W., Lister, G.S., 1991. Strain localization behaviour in experimental shear zones. Pure and Applied Geophysics 137, 421–438.

Jiang, D., White, J.C., 1995. Kinematics of rock flow and the interpretation of geological structures, with particular reference to shear zones. Journal of Structural Geology 17, 1249–1265.

Krantz, R.W., 1991. Measurements of friction coefficients and cohesion for faulting and fault reactivation in laboratory models using sand and sand mixtures. Tectonophysics 188, 203–207.

Kenis, I., Urai, J.L., van der Zee, W., Sintubin, M., 2004. Mullions in the High-Ardenne Slate Belt (Belgium): numerical model and parameter sensitivity analysis. Journal of Structural Geology 26, 1677–1692.

Kenis, I., Urai, J.L., van der Zee, W., Hilgers, C., Sintubin, M., 2005. Rheology of fine-grained siliciclastic rocks in the middle crust – evidence from structural and numerical analysis. Earth and Planetary Science Letters 233, 351–360.

Lamouroux, C., Debat, P., Inglès, J., Guerrero, N., Sirieys, P., Soula, J.C., 1994. Rheological properties of rock inferred from the geometry and microstructure in two natural shear zones. Mechanics of Materials 18, 79–87.

LaVision, 2005. StrainMaster 3D – Getting Started Manual for DaVis 7.1. LaVision GmbH, Goettingen.

Lohrmann, J., Kukowski, N., Adam, J., Oncken, O., 2003. The impact of analogue material properties on the geometry, kinematics, and dynamics of convergent sand wedges. Journal of Structural Geology 25, 1691–1711.

McClay, K., Bonora, M., 2001. Analog models of restraining stepovers in strike-slip fault systems. AAPG Bulletin 85, 233–260.

Means, W.D., 1984. Shear zones of types I and II and their significance for reconstruction of rock history. The Geological Society of America, 19th Annual Meeting, Abstracts with Programs, vol. 16, no.1, pp. 50.

Means, W.D., 1995. Shear zones and rock history. Tectonophysics 247, 157–160.

Mitra, G., 1979. Ductile deformation zones in Blue Ridge basement rocks and estimation of finite strains. Geological Society of America Bulletin 90, 935–951.

Mitra, G., 1984. Brittle to ductile transition due to large strains along the White Rock thrust, Wind River mountains, Wyoming. Journal of Structural Geology 6, 51–61.

Naylor, M.A., Mandl, G., Sijpesteijn, C.H.K., 1986. Fault geometries in basement-induced wrench faulting under different initial stress states. Journal of Structural Geology 8, 737–752.

Noveon, 1995. Carbopol Ultrez 10 polymer for personal care applications. Available from: www.personalcare.noveoninc.com/formulations/CarbopolUltrez10.asp

Paterson, M.S., 2001. Relating experimental and geological rheology. International Journal of Earth Sciences (Geologische Rundschau) 90, 157–167.

Poirier, J.P., 1985. Creep of Crystals. Cambridge University Press, New York, 260 pp.

Ramberg, H., 1962. Contact strain and folding instability of a multilayered body under compression. International Journal of Earth Sciences 51 (2), 405–439.

Ramsay, J.G., Graham, R.H., 1970. Strain variation in shear belts. Canadian Journal of Earth Sciences 7, 786–813.

Ramsay, J.G., 1980. Shear zone geometry: a review. Journal of Structural Geology 2, 83–99.

Ranalli, G., Fischer, B., 1984. Diffusion creep, dislocation creep, and mantle rheology. Physics of the Earth and Planetary Interiors 34, 77–84.

Regenauer-Lieb, K., Yuen, D.A., 2003. Modeling shear zones in geological and planetary sciences: solid- and fluid-thermal–mechanical approaches. Earth-Science Reviews 63, 295–349.

Riedel, W., 1929. Zur Mechanik geologischer Brucherscheinungen. Zentralblatt fuer Mineralogie, Geologie und Palaeontologie Abt. B, 354–368.

Schellart, W.P., 2000. Shear test results for cohesion and friction coefficients for different granular materials: scaling implications for their usage in analogue modelling. Tectonophysics 324, 1–16.

Schrank, C.E., Handy, M.R., Fusseis, F. Multiscaling of shear zones and the evolution of the brittle-to-viscous transition in continental crust. Journal of Geophysical Research, in press. doi:10.1029/2006JB004833.

Schmid, D.W., Podladchikov, Y.Y., Marques, F.O., 2004. Folding of a finite length power law layer. Journal of Geophysical Research 109, B03407. doi:10.1029/2003JB002421.2004.

Simpson, C., 1983. Displacement and strain patterns from naturally occurring shear zone terminations. Journal of Structural Geology 5, 497–506.

Sonder, L.J., 2001. Ductile shear zones as counterflow boundaries in pseudoplastic fluids: discussion and theory. Journal of Structural Geology 23, 149–153.

Talbot, C.J., 1999a. Can field data constrain rock viscosities? Journal of Structural Geology 21, 949–957.

Talbot, C.J., 1999b. Ductile shear zones as counterflow boundaries in pseudoplastic fluids. Journal of Structural Geology 21, 1535–1551.

Tchalenko, J.S., 1970. Similarities between shear zones of different magnitudes. Geological Society of America Bulletin 81, 1625–1640.

Treagus, S.H., Sokoutis, D., 1992. Laboratory modelling of strain variation across rheological boundaries. Journal of Structural Geology 14, 405–424.

Treagus, S.H., 1999. Are viscosity ratios of rocks measurable from cleavage refraction? Journal of Structural Geology 21, 895–901.

Treagus, S.H., Treagus, J.E., 2002. Studies of strain and rheology of conglomerates. Journal of Structural Geology 24, 1541–1567.

Weijermars, R., 1986. Flow behaviour and physical chemistry of bouncing putties and related polymers in view of tectonic laboratory applications. Tectonophysics 124, 325–358.

White, S.H., Burrows, S.E., Carreras, J., Shaw, N.D., Humphreys, F.J., 1980. On mylonites in ductile shear zones. Journal of Structural Geology 2, 175–187.